Journal of Thermal Science Vol.31, No.1 (2022) 120−129

https://doi.org/10.1007/s11630-022-1551-7 **Article ID: 1003-2169(2022)01-0120-10**

Transition from Unsteady Flow Inception to Rotating Stall and Surge in a Transonic Compressor

CAO Dongming, YUAN Caijia, WANG Dingxi*, HUANG Xiuquan

Shaanxi Key Laboratory of Internal Aerodynamics in Aero-Engines, Northwestern Polytechnical University, Xi'an 710072, China

Abstract: Since the transition from rotating stall to surge in a transonic compressor at high speed is very quick, quite often there is no time to take measures to prevent the surge. Therefore, it is desired to find any rotating stall precursors, of which the occurrence can offer sufficient time for stall or surge prevention. In this study, a series of unsteady flow analyses were performed on a transonic compressor under operating conditions before rotating stall with unsteady results scrutinized to find rotating stall precursors. Particular attention is paid to the spatial modes and time modes of static pressure near the casing and around the blade leading and trailing edges. The results show that the characteristics of the precursor in both spatial and time domains can be used as rotating stall warnings.

Keywords: transonic compressor, unsteady flow, precursor, rotating stall, surge

1. Introduction

It is well known that rotating stall and surge are the major aerodynamic stability problems in compressors [1]. To prevent rotating stall and surge, the early detection of the stall phenomenon is vitally important. However, this task is particularly difficult in a transonic compressor at a high speed for which the transition from rotating stall to surge is sudden and fast. For rotating stall, two different rotating stall inception mechanisms have been proposed in Refs. [2, 3], for which two common flow breakdown sequences are identified: the first is associated with a short length scale disturbance known as a 'spike', and the second is with a long length scale disturbance known as a 'modal oscillation'.

In early years, it is difficult to perform full-annulus unsteady simulations to model the rotating stall. Most researches were based on experimental study [4, 5] and reduced order approximation methods [6]. In recent years, high resolution experiments [7] and large-scale numerical simulations [8–12], including simulations for full-annulus multi-stage compressors have been used to study stall behavior. It is found that spillage of tip leakage flow upstream of the leading edge and the sudden growth of casing corner separation blockage are the two mechanisms at the origin of stall inception [8]. The studies mainly focus on the rotating stall characteristic and its inception in both low speed/high speed fans/compressors. Researches reported in these papers show that there are only few revolutions from spike stall inception to fully developed rotating stall. Thus, there is a need to understand the flow mechanism at the operating points before rotating stall inception occurs.

Apart from the researches on rotating stall inception, there are also quite a few researches on the unsteady flow behaviors aiming to find precursors for stall and surge.

Article type: Contributed by Asian Congress on Gas Turbines 2020 (August 18–19, 2021, China).
Received: Oct 15, 2021 Corresponding author: WANG Dingxi E-mail: dingxi_wang@nwpu.edu.cn

Some researches show that the unsteady flow near the tip region can have a great influence on the aerodynamic stability of the compressors. Zhiting Tong et al. studied the development of the three modes of tip leakage vortices in spike stall inception experimentally, and tip injection was used to gain the extension of stable operating range [13]. For a multi-row compressor, a strong periodical interaction between the incoming stator wakes and the rotor blade tip clearance vortices was observed [14]. Most experimental studies focused on the pressure characteristic at different locations on the casing. Different correlation methods were used to analyze the pressure signals from transducers which were arranged circumferentially on a casing for stall precursors, which could also detect deteriorated tip clearances and monitor individual blades [15, 16]. Similarly, the precursor of a rotating stall was detected by monitoring the collapse of the periodicity in the pressure fluctuation on the casing wall [17]. Temporal low-pass and band-pass filtering, temporal and spatial Fourier transforms including power-spectral-density calculations of the spatial coefficients, and a wavelet analysis technique were also used in stall inception measurements in the compressor system of a two-spool turbofan engine at various power settings [18]. There is also a computational model developed for simulating the development of both long and short-wavelength compressor instabilities [19].

In the open literature, few researches are found to compare the unsteady flow characteristic at different operating points to find any precursors for rotating stall using full-annulus unsteady simulations. Most studies focus on specific operating points with unsteadiness or the inception of the rotating stall, and little is known about the transition from unsteady flow inception to rotating stall inception. In this paper, full-annulus unsteady simulations are performed at the operating points from unsteady flow inception to rotating stall, aiming to find out the precursors for rotating stall at an early time.

The paper is organized as follows. The research subject, CFD (Computational fluid dynamics) methodology and overall performance are introduced in order first. The spatial harmonic characteristic and time frequency characteristic of the unsteady flow are analyzed at different unsteady operating points to find out the precursors for rotating stall. Then the transition of unsteady flow to rotating stall and surge is introduced. The last section draws the conclusion.

2. Research Subject

In this research, a widely used transonic fan rotor, NASA Rotor67 [20], is chosen as the research subject. Some of the fan design parameters are shown in Table 1.

Table 1 The design parameters of NASA Rotor67

Parameter	Value
Blade count	22
Aspect ratio	1.56
Tip clearance size	0.1016 cm
Design rotational speed	16 043 r/min
Design pressure ratio	1.63
Design mass flow rate	33.25 kg/s

3. CFD Methodology

The simulations presented in this paper are performed by Turbostream [21], which is a structured multi-block unsteady Reynolds-averaged Navier-Stokes (U-RANS) solver running on graphics processing unit (GPU) clusters. The governing equations are shown below:

$$\frac{\partial}{\partial t}\int_V U\mathrm{d}V = -\int_A C\cdot\boldsymbol{n}\mathrm{d}A + \int_A D\cdot\boldsymbol{n}\mathrm{d}A + \int_V S\mathrm{d}V$$

where U denotes the conserved variables; C denotes the convective flux, D denotes the diffusive flux; S denotes the source terms and $\boldsymbol{n}$ is a unit vector normal to the face area dA. For a steady state simulation, Turbostream uses an explicit time-stepping method called the 'Scree' scheme:

$$\Delta\boldsymbol{U} = \left(2\frac{\partial\boldsymbol{U}}{\partial t}\bigg|_n - \frac{\partial\boldsymbol{U}}{\partial t}\bigg|_{n-1}\right)\Delta t$$

where the subscripts refer to the time steps that the derivatives are evaluated at. For time-accurate simulations, turbostream uses the dual time-stepping method proposed by Jameson [22]. Based on the previous researches on the influence of inlet distortion on NASA Rotor67 and fan instability using Turbostream, it is found that good agreement between numerical results and experimental data can be obtained using the Spalart-Allmaras (SA) turbulence model. Therefore, the SA turbulence model is used to perform all simulations presented in this paper.

Subsonic inlet and outlet boundary conditions (total pressure and total temperature at the inlet, static pressure at the outlet) are used. Solver settings are the same for all steady simulations at different operating points, so are the unsteady simulations to make the results comparable.

4. CFD Setup and Overall Performance

As the case is a transonic compressor, the flow field at a near stall operating point can be quite sensitive to boundary conditions. To reduce the influence of boundary conditions on the flow field, the inlet and outlet of the computation domain are extended by 1 and 1.5 times the fan diameter, respectively. A single passage computational domain is used for steady simulations; a

full-annulus computational domain is used for time-accurate simulations, which is shown in Fig. 1. The grids used in this paper are generated by NUMECA/AUTOGRID5 with a multi-block O4H topology. Three grids with 1 million (45×77×239, without the refined grid in the O-mesh), 2 million (53×109×307, without the refined grid in the O-mesh), and 3 million (61×137×323, without the refined grid in the O-mesh) nodes per passage are used for the grid independence study. Fig. 2 shows two different views of the medium grid with 2 million nodes per passage.

For analyses approaching stall, the outlet back pressure is always increased with a small step size [23] or using a throttle model [24, 25] at the outlet. Pullan [8] and Mehdi [12] set a converged nozzle at the computational domain outlet to reduce the sensitivities of the outlet boundary condition. In this paper, a similar approach is used to simulate the stall process.

The speed lines calculated using the three grids and experimental data are shown in Fig. 3, with the same solver settings being used. The mass flow rate is normalized by their respective choke mass flow rate: the measured and calculated choke mass flow rates are 34.96 kg/s and 34.2 kg/s, respectively. Each grid has a nozzle applied at the outlet boundary and the speed line is obtained by gradually decreasing the nozzle outlet area. It shows that the medium grid can achieve a good balance between the computation cost and accuracy. Therefore, the medium grid is used to conduct all the simulations in this paper.

The whole speed line, which consists of results of steady and unsteady analyses using the medium grid, is shown in Fig. 4. The mass flow rate is normalized in the same way as that for the grid independence study. The speed line consists of three parts. The black part on the right is obtained by steady simulation by varying back pressure (without nozzle). The blue part is obtained from steady simulation, by gradually decreasing the nozzle outlet area with back pressure setting to the inlet total pressure. The red part is obtained from unsteady

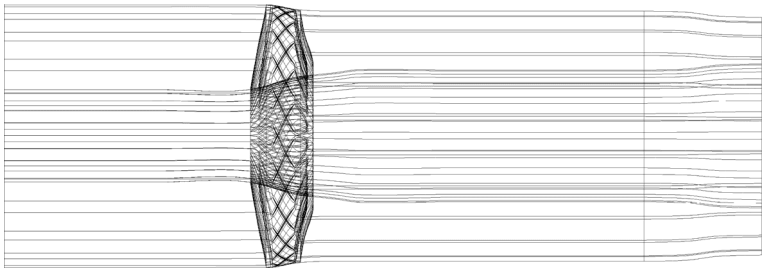

Fig. 1 Computational domain for unsteady simulations

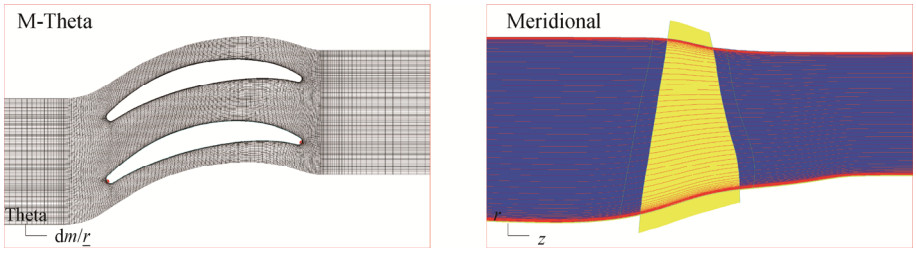

Fig. 2 The grid of NASA Rotor 67 with 2 million nodes

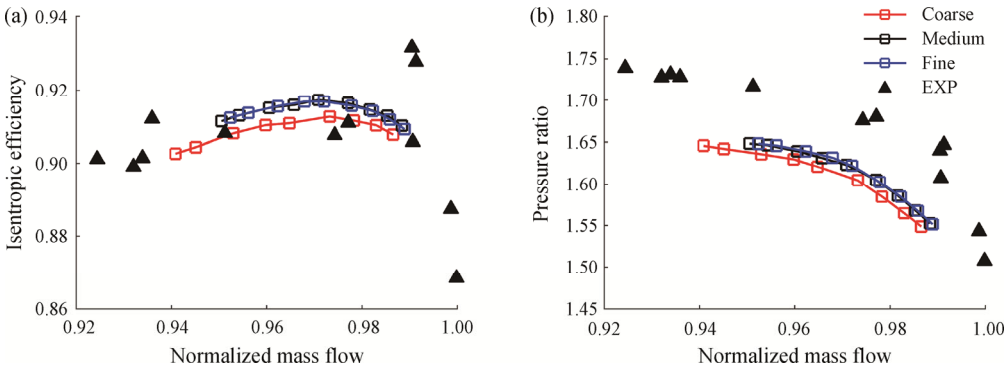

Fig. 3 Speed lines for grid independence study

simulation, by adjusting the nozzle area in the same way as that for the blue part. The discrepancy between numerical results and experimental results is not uncommon and is considered reasonable when referring to numerical analysis results reported in the open literature.

For all the steady simulations, it takes about one day using a GPU workstation with 8 K80 Cards. For time-accurate simulations, 100 physical time steps per fan blade passing period have been used for time integration, and nearly three revolutions can be modelled on the same GPU workstation per day.

The detailed flow coefficient and their corresponding aerodynamic performance from unsteady simulations are listed in Table 2. In the next section, detailed comparisons of flow field of these operating points are presented.

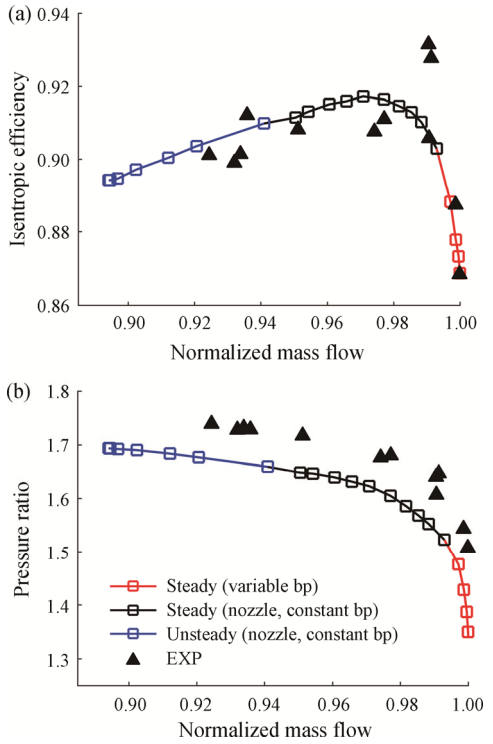

Fig. 4 Speed line for the NASA Rotor67 obtained using the medium grid

Table 2 The performance parameters from unsteady simulations

Flow coefficient	Pressure ratio	Label
0.940 98	1.6592	P1
0.920 64	1.6765	P2
0.912 10	1.6835	P3
0.902 36	1.6900	P4
0.896 78	1.6920	P5
0.894 56	1.6930	P6
0.894 13	1.6937	P7

5. Spatial Characteristics

For the first operating point (P1) presented in Table 2, the flow is almost steady and there is no difference between passages. Fig. 5 shows the static pressure distribution at a near casing area for P1. The red line in Fig. 5 shows the axial locations of numerical probes, which are set in front of the blade leading edge near the casing in each passage for the analysis presented later.

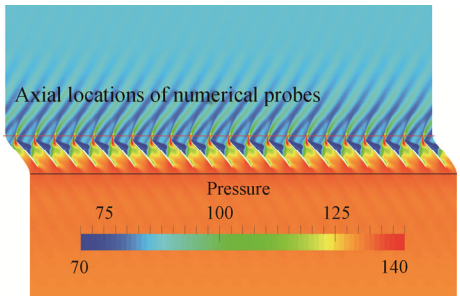

Fig. 5 Static pressure distribution near the casing at P1

At the axial positions near the blade leading edge and trailing edge (two lines in Fig. 5), three different spans are chosen to perform spatial DFT (Discrete Fourier transform) analysis on static pressure, the results at P1 are shown in Fig. 6, where LE refers to the leading edge and TE refers to the trailing edge.

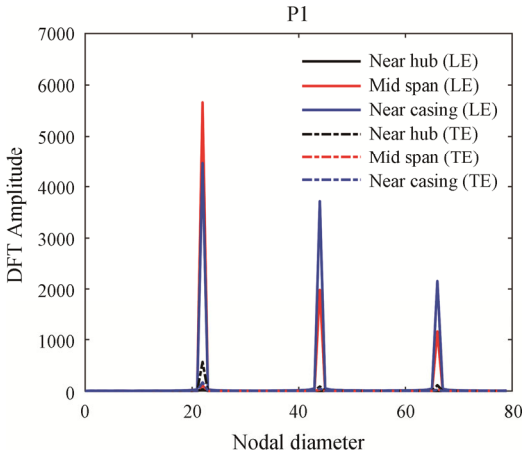

Fig. 6 DFT results of static pressure at P1

In Fig. 6, the major components are all from LE and the components from TE are relatively smaller, without any low nodal diameter components. The component in solid dark blue is from the leading edge near the casing. It is caused by the shock wave, which implies that the strength of the shock wave near the blade tip is quite strong for the transonic compressor.

From the operating point P1, the nozzle area was gradually reduced to get the next six operating points, which are P2 to P7. Fig. 7 shows the spatial DFT results

of static pressure of P2 to P7 at three different spans of the two axial planes as marked in Fig. 5. In Fig. 7, a low nodal diameter component occurs at all operating points, which is thought to be the precursor of a rotating stall. Further analyses of this precursor in both spatial and time domain at different operating points will be carried out below.

At operating point P2, the component with one nodal diameter appears only near the casing region at both the leading edge and trailing edge. When the operating point gradually moves to the stall boundary, the nodal diameter of this component increases except for P3 which has a nodal diameter of four. The energy (indicated by the corresponding amplitude) of this low nodal diameter also increases, which means that the unsteadiness becomes stronger. The components from the interference between the low nodal diameter component and the main flow (the nodal diameter is a multiple of the blade count) are also observed.

One interesting phenomenon is that, at the last two stable unsteady operating points P6 and P7, a new component with one nodal diameter appears, which means a new circumferential wave with a low nodal diameter occurs. The new component is thought to be a warning for rotating stall. In the next section, the frequency characteristics of these components with low nodal diameters are analyzed to corroborate that these flow components are stall precursors.

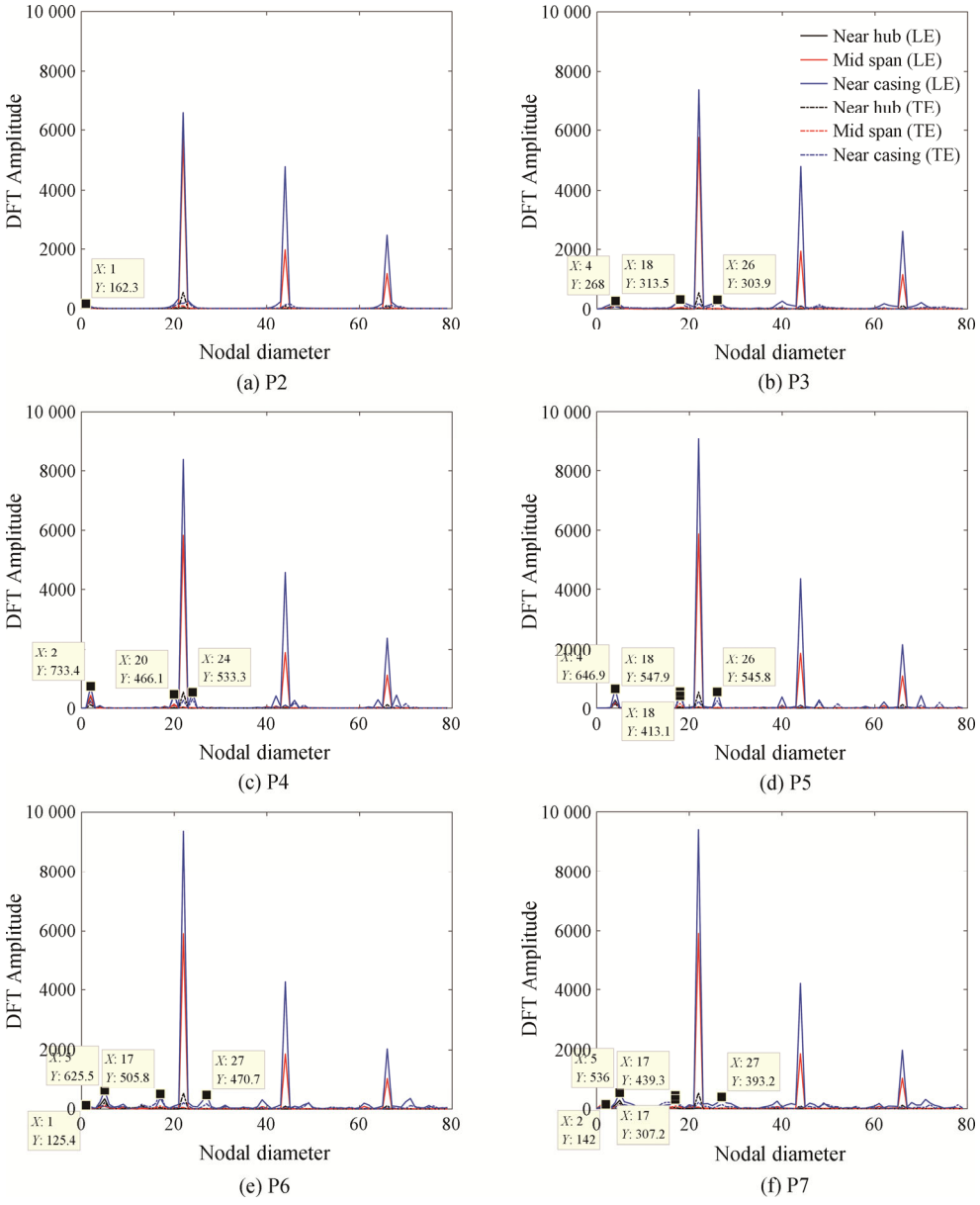

Fig. 7 DFT results of static pressure at 6 different unsteady operating points

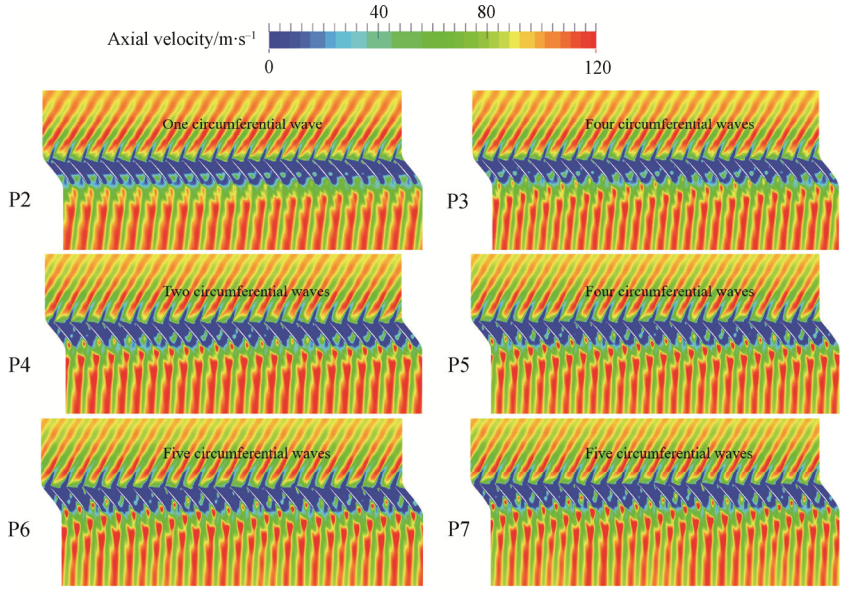

Fig. 8 Axial velocity distribution near the casing for operating points P2 to P7

As it is difficult to identify the nodal diameter pattern from static pressure contours, Fig. 8 shows the axial velocity distribution at a near casing region for operating points P2 to P7. The low nodal diameter at each operating point is related to the circumferential wave number of the disturbances, which results from the tip leakage flow near the blade leading edge. The tip leakage flow starts at the blade leading edge and then propagates and develops in the passage, which leads to the unsteadiness. When the solution at each operating point becomes stable (periodic over time), the circumferential disturbances caused by the tip leakage flow at the blade leading edge are uniformly distributed in the annulus. The circumferential positions of the tip leakage flow are not stationary in the rotating frame of reference, which means the tip leakage flow is rotating relative to the rotor blade. The rotating characteristic will be discussed in the next section.

6. Frequency Characteristics

Fig. 9 shows the static pressure histories from different passages over 9 revolutions for P2. The static pressure is taken from the blade leading edge near the casing as marked in Fig. 5. It can be seen that the static pressure histories from different passages have a phase difference, though the phase difference is not big. The phase difference in static pressure implies that the disturbance is travelling in the rotating frame of reference. Though not shown here to avoid redundancy, static pressure time histories of other operating points also show the same features of phase difference.

To get the frequency characteristics of the unsteady flow near the casing, wavelet analyses are performed to

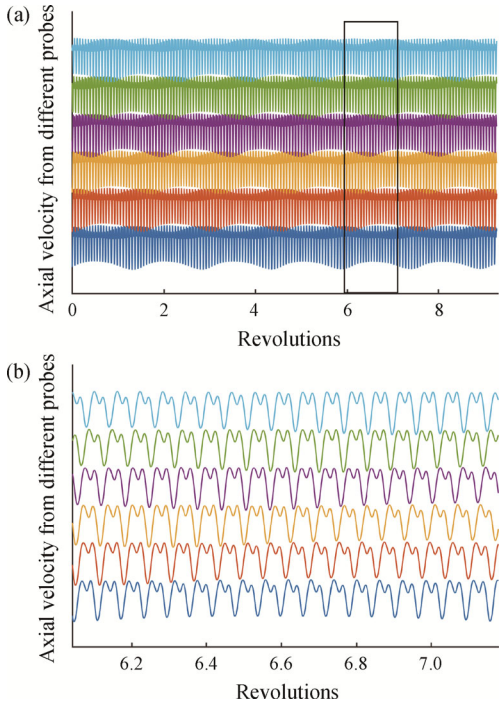

Fig. 9 Static pressure history from different passages over 9 revolutions for P2

the static pressure recorded by the numerical probes. Since the flow at different passages is periodic in time, the static pressure history from one specific passage is used. Fig. 10 shows the wavelet analysis results of the static pressure from operating points P2 to P7. The amplitude of the major frequency component increases when the operating point gradually moves to the stall boundary, which implies the strength of the tip leakage flow is growing. At P6 and P7, a low frequency

component emerges, and its frequency reduces when the operating point is pushed closer to the stall boundary. This low frequency component is considered the same component found in the spatial characteristic analyses. The comparability of the frequency of this flow component with that of rotating stall corroborates that it is a stall precursor.

For different operating points, the number of circumferential waves or the nodal diameter of the low frequency component is different. The frequency of the disturbances in a stationary frame of reference can be calculated by:

$$F_{\text{stationary}} = -F_{\text{rotating}} + \omega_{\text{r}} \times N \tag{1}$$

where $F_{\text{stationary}}$ refers to the frequency of disturbances in a stationary frame of reference; F_{rotating} refers to the frequency obtained by a wavelet analysis and can be understood as the frequency obtained when standing on a rotor blade; ω_{r} refers to the shaft speed; N refers to the number of the disturbances in the circumferential direction. The sign in the above equation means that the disturbances rotate in a direction opposite to the rotation of the rotor blade. The rotating speed of the disturbances in the stationary frame of reference can be calculated by:

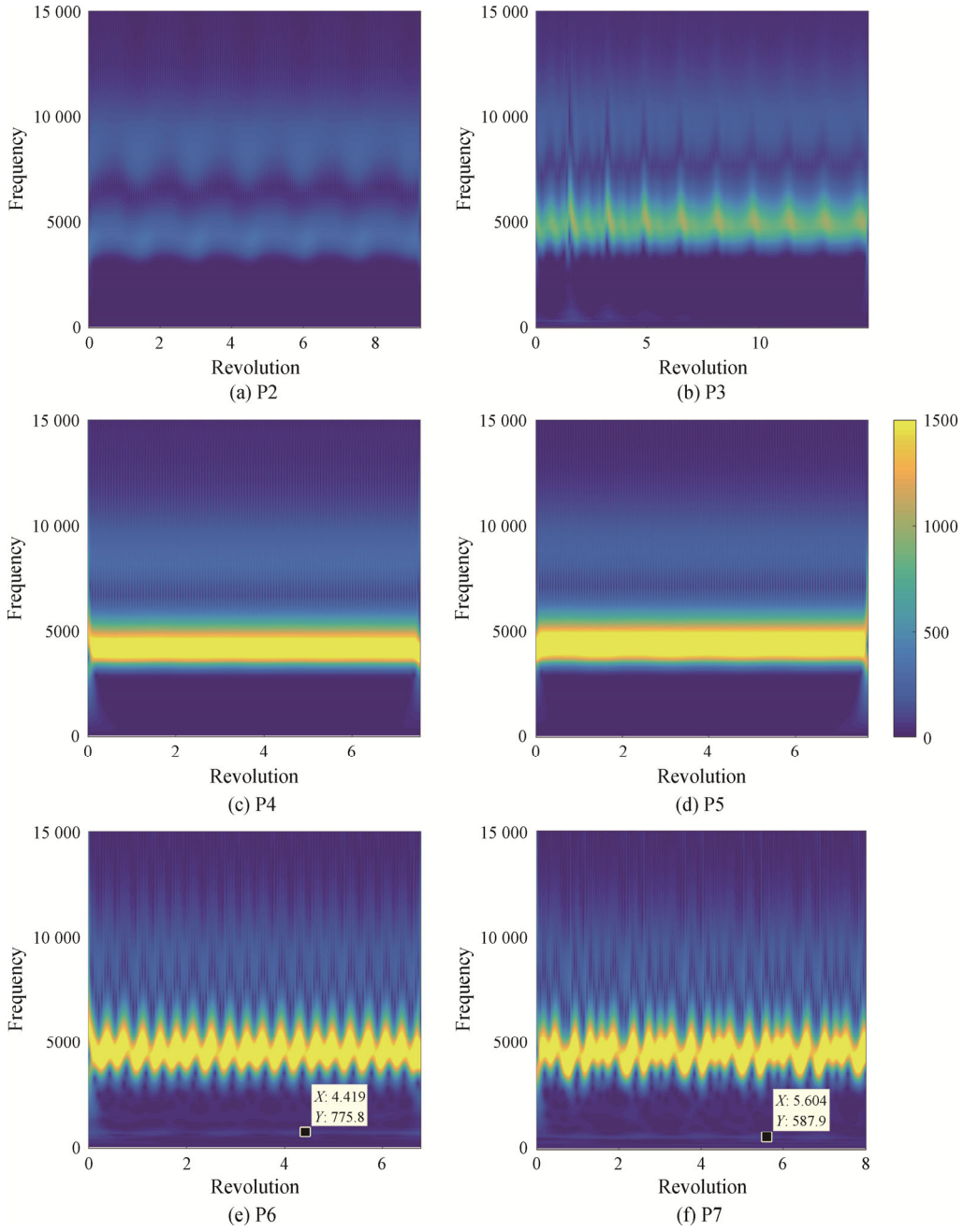

Fig. 10 Wavelet analysis results of the static pressure from P2 to P7

$$V_{\text{stationary}} = F_{\text{stationary}} / N \quad (2)$$

where $V_{\text{stationary}}$ refers to the rotating frequency of the disturbances in a stationary frame of reference. Fig. 11 shows the rotating speed of the disturbances at different operating points, which are normalized by shaft speed. The rotating speed of a disturbance reduces with the increase of the wave number, which can be seen as another warning for rotating stall.

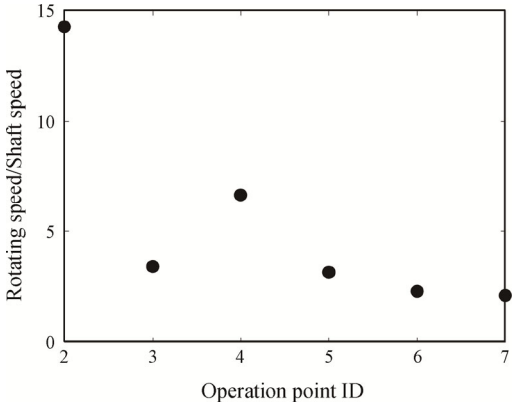

Fig. 11 Rotating speed of the disturbances at P2 to P7

7. Rotating Stall Analyses

For a transonic compressor, it is known that the operating range with a stable rotating stall is very small, and thus there is little time to take action to prevent the surge. From operating point P7, the nozzle area is further decreased by 0.04%; then the stable operating point P7 will be pushed into rotating stall and quickly develops into surge. Fig. 12 shows the axial velocity histories from the numerical probes for the stall point. As the flow field near the casing is transonic, it can be quite sensitive to the variation of the operating condition. When the solution diverges numerically, it means the compressor is surging. It can be seen that rotating stall and surge develops from a stable operating point in 20 revolutions.

Fig. 13 shows the axial velocity distributions near the casing at different revolutions before surge. One disturbance in the circumferential direction firstly expands to several passages, which can be seen at T=11 revolutions and T=16 revolutions, and then it further develops to cover a wider circumferential region at T=18 revolutions. The disturbance develops in both size and strength quickly, becoming one rotating stall cell as

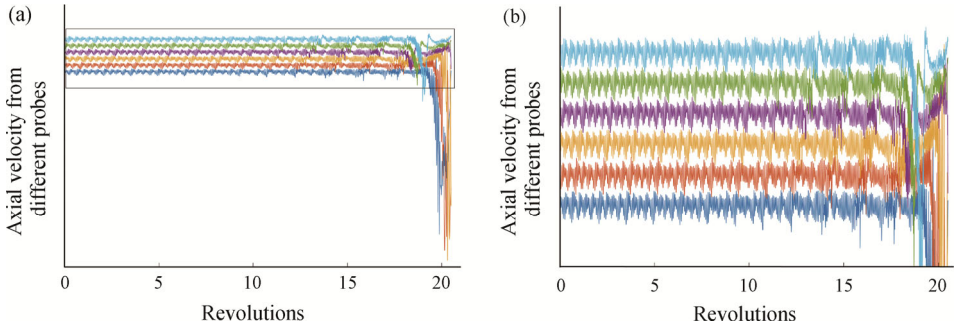

Fig. 12 Axial velocity history from different passages at the stall point

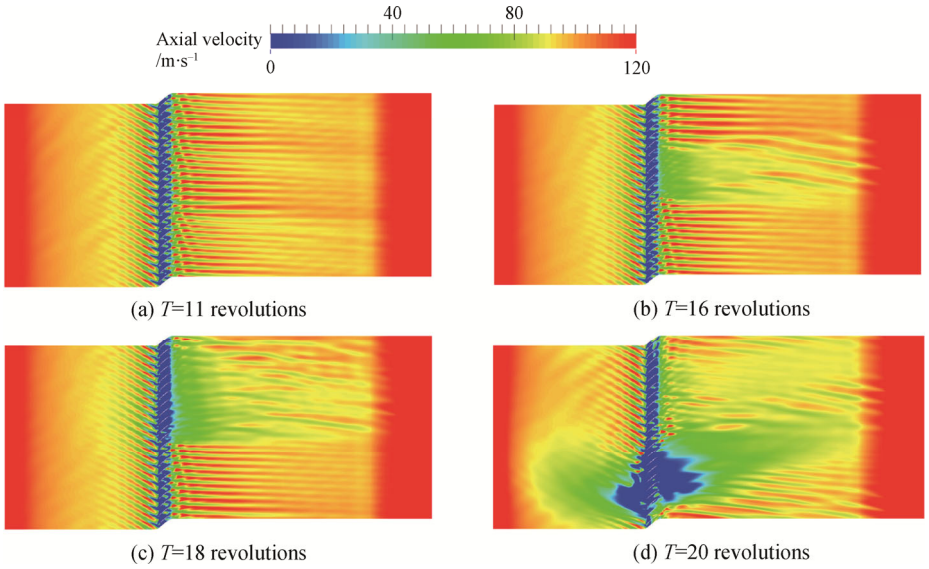

Fig. 13 Axial velocity distributions near the casing at different revolutions

shown at T=20 revolutions. The rotating stall mainly occupies the span region above 60% as shown in Fig. 14. As the flow field at the tip region is transonic, the operating range with stable rotating stall can be quite small. The compressor will quickly develop into surge after rotating stall occurs. In this study, the flow solution diverges numerically after 20 revolutions, indicating surge occurs.

The frequency characteristic of the stall cell is then analyzed. The flow is developing from a stable unsteady operating point P7 to rotating stall, and the flow field varies greatly with time. A wavelet analysis is performed on the axial velocity recorded by the numerical probes. Fig. 15 shows the wavelet analysis results for the axial velocity near the casing before the blade leading edge and one major frequency component is 137.1 Hz. According to Eq. (1) and Eq. (2), the rotating speed of the stall cell is 48.72% of the shaft speed.

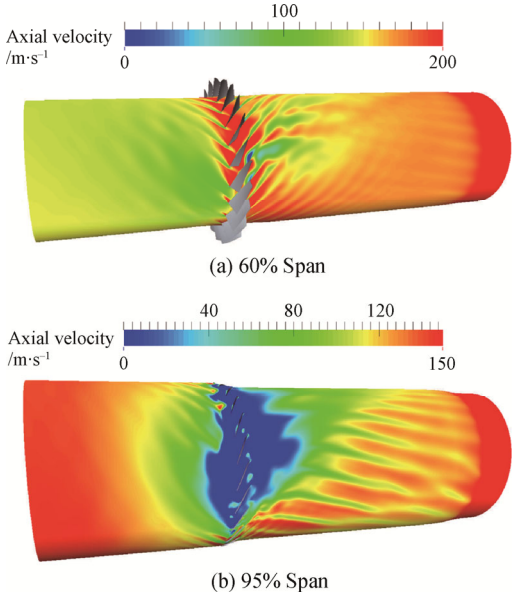

Fig. 14 Rotating stall cell at different spans

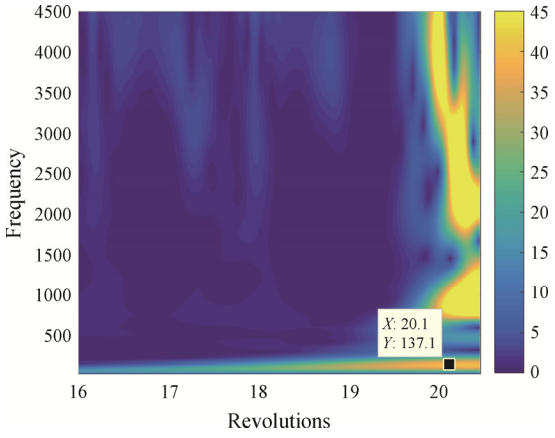

Fig. 15 Wavelet analysis results for the axial velocity at the stall point

8. Conclusions

In this paper, full-annulus unsteady analyses have been performed on a transonic rotor at different operating points near stall. Comparing the results from different operating points, the following conclusions can be drawn:

(1) There is a wide range between unsteady flow inception and rotating stall in a transonic compressor at a high speed, but the range between rotating stall and surge is quite small.

(2) From the spatial harmonic characteristic analysis of the static pressure at both the blade leading edge and trailing edge, apart from the components of shock wave at the tip region, there exists the component with a low nodal diameter. The low nodal diameter flow component is found to be caused by the tip leakage flow near the blade leading edge. This low nodal diameter component is considered the precursor of rotating stall. The first warning for rotating stall is that the increase of the nodal diameter and amplitude of the precursor and the occurrence of another low nodal diameter component.

(3) Based on the frequency characteristic analyses of the precursor at different points, the second warning is the reduction in the rotating speed of the circumferential waves caused by the tip leakage flow and the strength enhancement of the tip leakage flow. At the same time, there will be a low frequency component found at the last two unsteady operations, and the frequency of which is decreasing when the operating point is pushed closer to the stall boundary. The existence of this low frequency component is considered the third waring for rotating stall.

(4) A one-cell part-span rotating stall is found, rotating at the speed of 48.72% of the shaft speed. As the flow near the tip is transonic, the disturbances grow rapidly. The solution diverges at last, which is considered that the fan is surging.

Acknowledgements

The research was supported by the National Natural Science Foundation of China under Grant No. 51976172, National Science and Technology Major Project (2017-II-0009-0023), and China's 111 project under Grant No. B17037.

References

[1] Day I.J., Stall, surge, and 75 years of research. Journal of Turbomachinery, 2016, 138(1): 011001–011016.

[2] Camp T.R., Day I.J., A study of spike and modal stall phenomena in a low-speed axial compressor. Proceedings of the ASME 1997 International Gas Turbine and

Aeroengine Congress and Exhibition, Orlando, Florida, USA, June 2–5, 1997, 97-GT-526, V001T03A109. DOI: 10.1115/97-GT-526.

[3] Tan C.S., Day I.J., Morris S., Wadia A., Spike-type compressor stall inception, detection and control. Annual Reveal of Fluid Mechanics, 2010, 42: 275–300.

[4] Freeman C., Wilson A.G., Day I.J., Swinbanks M.A., Experiments in active control of stall on an aeroengine gas turbine. Journal of Turbomachinery, 1998, 120(4): 637–647.

[5] He L., Computational study of rotating-stall inception in axial compressors. Journal of Propulsion and Power, 1997, 13(1): 31–38.

[6] Yue S., Wang Y., Wei L., et al., Experimental investigation on the development process of large-scale low-speed stall disturbance in contra-rotating compressor. Journal of Thermal Science, 2020, 29(5): 1282–1291.

[7] Kim S., et al., Stall inception in low pressure ratio fans. Journal of Turbomachinery, 2019, 141(7): 071005–071013.

[8] Crevel F., Gourdain N., Moreau S., Numerical simulation of aerodynamic instabilities in a multistage high-speed high-pressure compressor on its test-rig—part I: rotating stall. Journal of Turbomachinery, 2014, 136(10): 101003–101016.

[9] Hewkin-Smith M., Pullan G., Grimshaw S.D., et al., The role of tip leakage flow in spike-type rotating stall inception. Journal of Turbomachinery, 2019, 141(6): 061010–061019.

[10] Dodds J., Vahdati M., Rotating stall observations in a high speed compressor—part ii: numerical study. Journal of Turbomachinery, 2015, 137(5): 051003–051012.

[11] Tong Z., et al., The self-induced unsteadiness of tip leakage vortex and its effect on compressor stall inception. Proceedings of the ASME Turbo Expo 2007: Power for Land, Sea, and Air, Montreal, Canada, May 14–17, 2007, pp. 1551–1562. DOI: 10.1115/GT2007-27010.

[12] Mailach R., Lehmann I., Vogeler K., Periodical unsteady flow within a rotor blade row of an axial compressor—part ii: wake-tip clearance vortex interaction. Journal of Turbomachinery, 2008, 130(4): 041005–041014.

[13] Dhingra M., Neumeier Y., Prasad J.V.R., et al., Stall and surge precursors in axial compressors. 39th AIAA/ASME/SAE/ASEE Joint Propulsion Conference and Exhibit, 2003. DOI: 10.2514/6.2003-4425.

[14] Bright M.M., et al., Stall precursor identification in high-speed compressor stages using chaotic time series analysis methods. Journal of Turbomachinery, 1997: 491–499.

[15] Inoue M., Kuroumaru M., Iwamoto T., et al., Detection of a rotating stall precursor in isolated axial flow compressor rotors. Journal of Turbomachinery, 1991, 113(2): 281–287.

[16] Hoss B., Leinhos D., Fottner L., Stall inception in the compressor system of a turbofan engine. Journal of Turbomachinery, 2000, 122(1): 32–44.

[17] Gong Y., Tan C.S., Gordon K.A., et al., A computational model for short-wavelength stall inception and development in multistage compressors. Journal of Turbomachinery, 1999, 121(4): 726–734.

[18] Strazisar A.J., Wood J.R., Hathaway M.D., et al., Laser anemometer measurements in a transonic axial-flow fan rotor. Journal of Engineering for Gas Turbines and Power, 1981, 103(2): 430–437.

[19] Brandvik T., Pullan G., An accelerated 3d Navier-Stokes solver for flows in turbomachines. Journal of Turbomachinery, 2011, 133(2): 021025.

[20] Jameson A., Time dependent calculations using multigrid, with applications to unsteady flows past airfoils and wings. 10th Computational Fluid Dynamics Conference, 1991. DOI: 10.2514/6.1991-1596.

[21] Peng S., Guang W.F., Ye J.Z., Numerical research of spike-like stall feature on transonic compressor. Journal of Engineering Thermophysics, 2018, 39(01): 76–81. (in Chinese)

[22] Zi W.W., Dong J.L., Ti C., Numerical simulation of the rotating stall feature on a single stage transonic compressor. Physics of Gases, 2021, 6(01): 30–37. (in Chinese)

[23] Bing C., Zuo L.X., Research on rotating stall of transonic compressor rotor based on constrained large eddy simulation method. Abstracts of the 11th National Conference on Fluid Mechanics, 2020. DOI: 10.26914/c.cnkihy.2020.035764. (in Chinese)